# Interferometric imaging of surface acoustic waves on a glass sphere

P. H. Otsuka, O. Matsuda, M. Tomoda, and O. B. Wright[a)]
*Division of Applied Physics, Graduate School of Engineering, Hokkaido University, Sapporo 060-8628, Japan*

(Received 17 July 2010; accepted 17 October 2010; published online 20 December 2010)

We use an ultrafast optical pump and probe technique to investigate the propagation of subgigahertz surface acoustic waves on a 1 mm diameter glass sphere with an aluminum coating. A fiber-based pump setup generates the surface waves and a common-path interferometer images them in the time domain over the sphere surface as they pass through the pole opposite the source of excitation. Fourier analysis allows the acoustic spectrum of the acoustic source to be extracted and waves traveling in opposite directions to be isolated. © *2010 American Institute of Physics*.
[doi:10.1063/1.3517076]

## I. INTRODUCTION

The propagation of surface acoustic waves (SAWs) on curved surfaces plays a key role in fields such as sensing, nondestructive evaluation and seismology. For example, Clorennec and Royer[1,2] investigated SAWs traveling on polycrystalline metal cylinders and spheres using a focused pulsed laser source and interferometric probing at various points. Yamanaka *et al.*[3] piezoelectrically excited and detected SAWs on crystalline dielectric spheres, resulting in many acoustic round trips with low attenuation, and demonstrated applications in gas sensing. However, the ideal technique for characterizing SAWs on curved surfaces would be to image the acoustic wave packets as they travel. This has been done by imaging SAWs on spheres through changes in optical reflectivity caused by the photoelastic effect:[4,5] the vicinity of the source of excitation was probed as well as the opposite pole where thermal effects do not interfere with the measurements. In the latter case the spatial resolution was relatively low and no Fourier analysis was attempted. This photoelastic-based method gives rise to polarization effects, complicating the interpretation of the images and reducing the image symmetry.

In this study, we describe how a common-path optical interferometer[6,7] can be adapted to the two-dimensional (2D) imaging of transient out-of-plane motion of a curved surface. We thereby achieve real-time imaging of the surface motion induced by laser-generated SAWs on a glass sphere. By Fourier analysis of a temporal series of images, waves traveling in opposite directions are isolated and analyzed separately. The real and imaginary components of the source function that governs the acoustic spectrum are also derived.

## II. EXPERIMENT AND RESULTS

Our sample is a 1 mm diameter BK7 glass sphere (Meller Optics Inc.) coated with a thin polycrystalline aluminum film with surface roughness ~5 nm. A complete covering of the sphere was obtained by alternately sputtering each hemisphere. This resulted in a varying film thickness, whereby the coating is thickest at the poles (~60 nm) and thinnest at the equator. For surface wave generation and detection, we use an optical pump-probe technique with a common-path Sagnac interferometer.[6,7] SAWs are thermoelastically excited by optical pulses from a mode-locked Ti:sapphire laser with a wavelength of 830 nm, repetition rate of 80 MHz, duration of ~200 fs and incident pulse energy of ~0.5 nJ. To enable the sphere to rotate while keeping the pump spot fixed, the pulses pass through an optical fiber and a SELFOC® microlens (of diameter 1.8 mm and pitch 0.29), which are both fixed with the sphere to a biaxial rotation stage as shown in Fig. 1. The fiber is a nonpolarization-preserving silica monomode fiber with a cutoff wavelength of 750 nm, a core diameter of 5 $\mu$m and a numerical aperture of 0.11. The microlens is used to focus the fiber output beam at normal incidence to a spot of diameter ~4 $\mu$m on the sphere surface, exciting SAWs up to ~700 MHz. We estimate both the instantaneous and steady state temperature rises of the illuminated region to be ~200 K.

The probed region is on the opposite side of the sphere to the point of excitation. Out-of-plane motion is detected interferometrically by a pair of second-harmonic 415 nm optical pulses temporally separated by $\tau \approx 300$ ps and focused at normal incidence on the sphere surface to a spot diameter of ~2 $\mu$m with a ×50 objective lens. The optical phase difference $\Delta\phi$ between the two probe pulses is monitored,

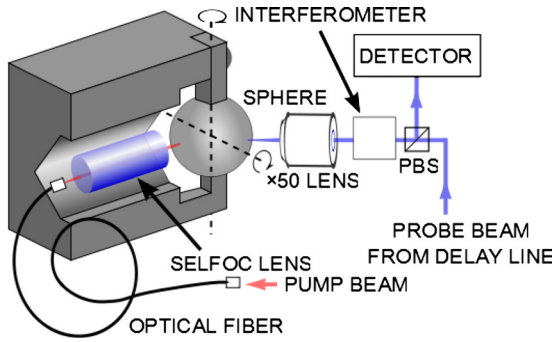


FIG. 1. (Color online) Schematic diagram of the setup. The entire sample stage rotates relative to the probe spot. The axis between the clamped points of the sphere is the fast scanning axis, corresponding to the $x$ axis in the recorded images.

a)Electronic mail: assp@kino-ap.eng.hokudai.ac.jp.

 

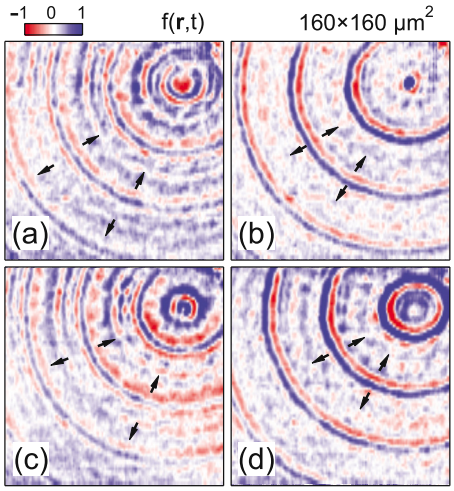


FIG. 2. (Color online) SAW images on a 1 mm glass sphere at times $t$ equal to (a) −3 ns, (b) 0 ns, (c) 3 ns, and (d) 6 ns. Waves traveling toward the pole in the upper right corner converge and then diverge as outward traveling waves.

thereby, allowing the out-of-plane surface velocity to be measured (since $\tau \ll 2\pi/\omega$, where $\omega$ is the SAW angular frequency). Detection sensitivity is improved by chopping the pump beam at 1 MHz and using a lock-in amplifier. We record a peak displacement ~1 pm. Each image is built up by two-axis rotation (here, $\sim \pm 10°$) of the sphere relative to the probe spot while keeping the pump beam focused on a fixed point on the sphere. We then vary the pump-probe delay time and build up an animation[8] of 29 frames (at a time separation of 0.431 ns) of the SAW propagation over the interval $T=12.5$ ns between successive laser pulses. During scanning the distance between the probe beam lens and the sphere is maintained constant to an accuracy of $\sim \pm 1$ $\mu$m.

The generated broadband SAW wavefronts propagate radially over the sphere from the pump spot, following the curvature of the sphere and initially converging toward the opposite pole. Figure 2 shows a series of SAW images, corresponding to $18.3° \times 18.3°$ or $160 \times 160$ $\mu m^2$, obtained at 3.0 ns intervals, with $t=0$ being defined as the moment of convergence at the pole [Fig. 2(b)]. At this time the peak-to-peak amplitude at the focus becomes ~4 times larger than for the outermost ring in Fig. 2(b). The $(x,y)$ coordinates in Fig. 2 correspond to $(a\theta_x, a\theta_y)$, where $a$ is the sphere radius and $(\theta_x, \theta_y)$ are the corresponding stage rotation angles. The images reveal two sets of waves: those converging toward the pole and those diverging away from it. In frames (b) and (d) the converging and diverging wave fronts overlap. Figure 3(a) is the equivalent time-distance plot, with the horizontal axis representing the radial distance from the pole in the $-x$ direction. The SAWs are not detected after a further full round trip. The literature value for the ultrasonic attenuation coefficient[9] of bulk longitudinal waves in the comparable material silica at 300 MHz, ~1 $cm^{-1}$, is sufficient to explain this, although other factors such as the presence of the aluminum film may also contribute.

## III. FOURIER ANALYSIS OF THE DATA

The acoustic dispersion relation and source characteristics can be derived from the experimental data by Fourier

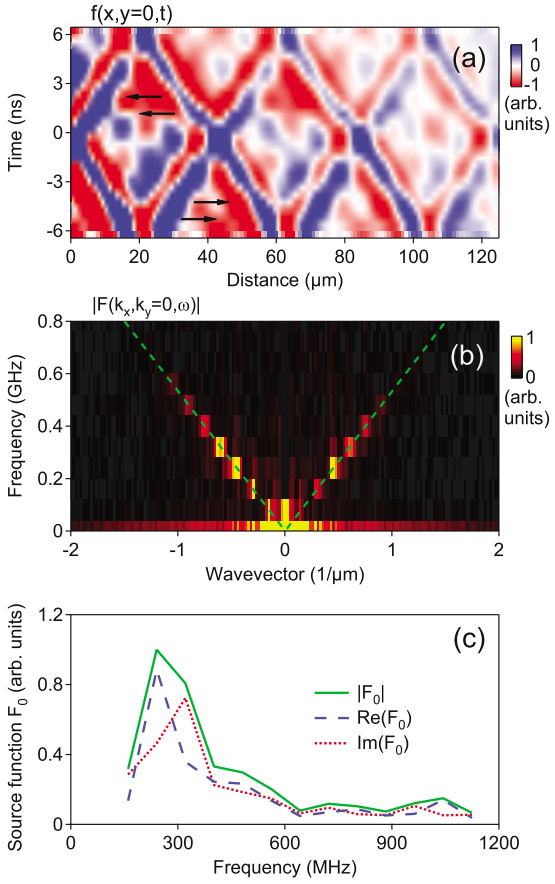


FIG. 3. (Color online) (a) Time-distance image of SAW propagation. The origin corresponds to the point of convergence at the imaged pole. Converging and diverging waves exhibit − and + gradients, respectively. (b) Cross-section $|F(\mathbf{k},\omega)|$ at $k_y=0$ of the spatiotemporal Fourier transform. Dashed line: theory. (c) Real (dashed), imaginary (dotted), and absolute (solid) components of the experimental source function $F_0(k)=F_0(\omega/v)$.

analysis.[7,10] The acoustic field $f(\mathbf{r},t)$ (where $\mathbf{r}$ represents the position $x=a\theta_x$ and $y=a\theta_y$ on the curved surface of the sphere), corresponding to $\Delta\phi$ in experiment, can be expressed for our small ($\pm 10°$) rotation angles as a combination of Fourier transforms in the spatial and temporal domains

$$f(\mathbf{r},t) = \int_{-\infty}^{\infty} F(\mathbf{k},\omega)\exp[i(\mathbf{k}\cdot\mathbf{r}-\omega t)]d^2\mathbf{k}d\omega, \quad (1)$$

where the Fourier amplitude $F(\mathbf{k},\omega)$ is given by

$$F(\mathbf{k},\omega) = \frac{1}{(2\pi)^3}\int_{-\infty}^{\infty} f(\mathbf{r},t)\exp[-i(\mathbf{k}\cdot\mathbf{r}-\omega t)]d^2\mathbf{r}dt. \quad (2)$$

Here, $\mathbf{k}$ is an effective 2D acoustic wave vector corresponding to $\mathbf{r}$. We may also express $f(\mathbf{r},t)$ by a superposition of acoustic eigenmodes. If we assume that only one acoustic branch with dispersion relation $\omega=\omega(\mathbf{k})$ is present, and that the sample is homogeneous, we may write

$$f(\mathbf{r},t) = \mathrm{Re}\int_{-\infty}^{\infty} F_0(\mathbf{k})\exp[i(\mathbf{k}\cdot\mathbf{r}-\omega(\mathbf{k})t)]d^2\mathbf{k}$$
$$= \frac{1}{2}\int_{-\infty}^{\infty}\{F_0(\mathbf{k})\exp[i(\mathbf{k}\cdot\mathbf{r}-\omega(\mathbf{k})t)] + F_0^*(\mathbf{k})\exp[-i(\mathbf{k}\cdot\mathbf{r}-\omega^*(\mathbf{k})t)]\}d^2\mathbf{k}$$
$$= \frac{1}{2}\int_{-\infty}^{\infty}\{F_0(\mathbf{k})\exp[i(\mathbf{k}\cdot\mathbf{r}-\omega(\mathbf{k})t)] + F_0^*(-\mathbf{k})\exp[i(\mathbf{k}\cdot\mathbf{r}+\omega^*(-\mathbf{k})t)]\}d^2\mathbf{k}. \quad (3)$$

Here, $F_0(\mathbf{k})$ is the complex amplitude of mode $\mathbf{k}$, so $F_0(\mathbf{k})$ can be considered as a source function that determines the spectral content of the acoustic mode.

If we assume that acoustic attenuation is negligible, i.e., that the whole system exhibits time-reversal symmetry, the relation $\omega(\mathbf{k})=\omega(-\mathbf{k})=\omega^*(\mathbf{k})$ holds.[10] In this case, substitution of Eq. (3) to Eq. (2) implies

$$F(\mathbf{k},\omega) = \frac{1}{2}\{F_0(\mathbf{k})\delta[\omega-\omega(\mathbf{k})] + F_0^*(-\mathbf{k})\delta[\omega+\omega(\mathbf{k})]\}. \quad (4)$$

For $\omega>0$, we obtain

$$F(\mathbf{k},\omega) = \frac{1}{2}F_0(\mathbf{k})\delta[\omega-\omega(\mathbf{k})]. \quad (5)$$

This equation directly connects the spatiotemporal Fourier amplitude and the source function. $F(\mathbf{k},\omega)$ takes a finite value only for combinations of $\mathbf{k}$ and $\omega$ which satisfy the dispersion relation $\omega=\omega(\mathbf{k})$. The function $F(\mathbf{k},\omega)$, therefore, allows access to the acoustic dispersion relation.

A cross section of the experimental value of $|F(k_x,k_y=0,\omega)|$ derived from the experimental animation, corresponding to the dispersion relation for propagating waves with $\theta_y=0$, is shown in Fig. 3(b).[11] The effect of the Al film on the acoustic dispersion for the propagation distances $\sim 200$ $\mu$m over the imaged region is negligible, although the cumulative effect of this dispersion for propagation from one pole of the sphere to the other may not be.[12,13] The derived phase velocity is $v\approx(3320\pm 60)$ ms$^{-1}$. To compare with theory, one should account for a small increase in the speed compared to the Rayleigh velocity $v_R$ due to the surface curvature[1,14,15]

$$v \approx v_R\left(1+\frac{\epsilon}{ka}\right), \quad (6)$$

where $\epsilon\approx 2.1$ depends on the elastic constants of BK7 (Ref. 16), $v_R=3350$ ms$^{-1}$ for this material[17] and $ka\gg 1$. For a typical frequency of 300 MHz, or $ka=300$, the correction is $\epsilon/ka\approx 0.007$, giving $v\approx 3370$ ms$^{-1}$. The dashed lines in Fig. 3(b), derived from Eq. (6), give good agreement with experiment. Although the speed correction from surface curvature is negligible, the effect of the dispersion is cumulative and gives rise to pulse inversion when the propagation angle around the sphere is approximately equal to 81°.[1] However, for propagation distances $\sim 200$ $\mu$m over the imaged region, corresponding to angles of $\sim\pm 10°$, this effect is relatively small. A first-principles calculation of the SAW pulse shape, that would require a knowledge of the film and curvature dispersions as well as the thermoelastic generation process,[18] is beyond the scope of this paper.

The profile of a circular wave front passing through a focus in 2D is known to undergo a shape change and a $\pi/2$ Gouy phase shift.[19,20] Our experimental resolution for $\Delta\phi$ allowed us to study the former effect in detail but not the latter. The change in shape is governed by the complex value of the source function $F_0$. Consider an acoustic field with inversion symmetry for which the relation $f(\mathbf{r},t)=f(-\mathbf{r},t)$ and thus $F_0(\mathbf{k})=F_0(-\mathbf{k})$ necessarily holds. By setting $F_0(\mathbf{k})=(1/2)F_0(\mathbf{k})+(1/2)F_0(-\mathbf{k})$ in the first line of Eq. (3) and then converting the second integral in this sum by the substitution $\mathbf{k}\rightarrow-\mathbf{k}$, we obtain

$$f(\mathbf{r},t) = \mathrm{Re}\int_{-\infty}^{\infty} F_0(\mathbf{k})\cos(\mathbf{k}\cdot\mathbf{r})\exp[-i\omega(\mathbf{k})t]d^2\mathbf{k}. \quad (7)$$

If $F_0$, which depends on the choice of time origin, is pure imaginary for a given wave packet, Eq. (7) becomes

$$f(\mathbf{r},t) = \int_{-\infty}^{\infty} -iF_0(\mathbf{k})\cos(\mathbf{k}\cdot\mathbf{r})\sin[\omega(\mathbf{k})t]d^2\mathbf{k}. \quad (8)$$

In this case the disturbance $f(\mathbf{r},t)$ thus completely vanishes for all $\mathbf{r}$ at the instant $t=0$.

As these concepts do not seem to be discussed in detail in the literature, before analyzing the experimental results we first show how a trial acoustic field changes on passing through a focus in 2D by means of a simulation. Figure 4 shows the results of calculations of the acoustic field over a $100\times 100$ $\mu$m$^2$ region for the case in which $|F_0(\mathbf{k})|$ is chosen in the form (roughly in accord with that found in experiment)

$$|F_0(\mathbf{k})| = \exp[-(k-k_0)^2/k_1^2][1-\exp(-2k/k_1)], \quad (9)$$

where $k=|\mathbf{k}|$, $k_0=0.45$ $\mu$m$^{-1}$, $k_1=0.3$ $\mu$m$^{-1}$ and the wave velocity is taken to be 3.3 km s$^{-1}$. The images in Figs. 4(a)–4(c) and sections below them correspond to the temporal evolution ($t=-10$ ns, 0, and 10 ns) of a wave packet for pure imaginary $F_0$ with a modulus defined by Eq. (9), for which $t=0$ is defined at the moment the wave packet passes through the focus. In this case $f(\mathbf{r},t)=0$ at $t=0$ [$\partial f(\mathbf{r},t)/\partial t$ is a maximum] and the diverging wave packet is inverted [$f(\mathbf{r},-t)=-f(\mathbf{r},t)$]. In contrast, if $F_0$ is real, Eq. (7) becomes

$$f(\mathbf{r},t) = \int_{-\infty}^{\infty} F_0(\mathbf{k})\cos(\mathbf{k}\cdot\mathbf{r})\cos[\omega(\mathbf{k})t]d^2\mathbf{k}. \quad (10)$$

In this case $f(\mathbf{r},t)$ is a maximum at $t=0$ [$\partial f(\mathbf{r},t)/\partial t=0$] and the converging and diverging wave packets are identical [$f(\mathbf{r},-t)=f(\mathbf{r},t)$]. This is demonstrated in Figs. 4(d)–4(f) for the same $|F_0(\mathbf{k})|$ as in (a)–(c). In general $F_0$ will have both real and imaginary components and the shape of the converging and diverging wave packets will be different.[20] Since $ka\gg 1$, our case of wave fronts on an isotropic sphere over a limited range of angles $\theta_x$ and $\theta_y$ is essentially the same as this 2D case.

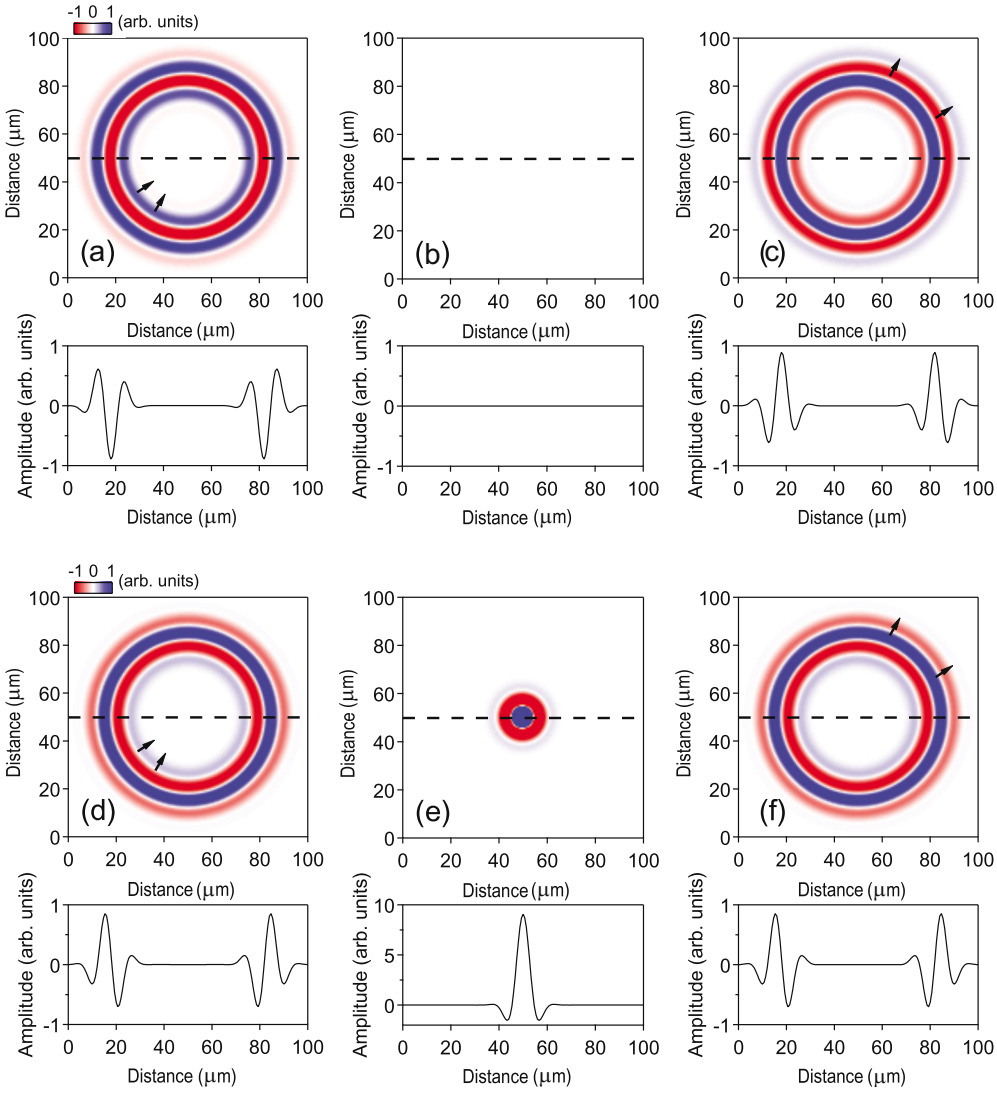


FIG. 4. (Color online) An example of simulated SAW images for $f(\mathbf{r},t)$ at times $t$ equal to [(a) and (d)] −10 ns, [(b) and (e)] 0 ns, and [(c) and (f)] 10 ns. The sections below the images show the amplitude along the corresponding dashed lines. (a)–(c) correspond to a pure imaginary source function $F_0$, whereas (d)–(f) correspond to the pure real case.

Use of Eq. (5) allows the determination of the absolute value and the real and imaginary parts of $F_0(\mathbf{k})=F_0(|\mathbf{k}|)=F_0(\omega/v)$ in experiment, as shown in Fig. 3(c),[21] indicating SAW excitation in the range ~100–700 MHz with a peak at ~300 MHz, largely determined by the size of the optical pump spot. We find that $\mathrm{Re}(F_0)\sim\mathrm{Im}(F_0)$. This is presumably the result of the thermoelastic generation conditions and subsequent pulse reshaping on propagation round the sphere. For other films and substrates and in the vicinity of the excitation point we have previously observed $\mathrm{Im}(F_0)$ to be predominant.[7,10] To better ascertain the effect on the wave packet shape, we have separated converging and diverging waves by (1) spatiotemporal Fourier transforming, (2) masking the unwanted wave vectors for the relevant propagation directions, and (3) inverse Fourier transforming. Typical images obtained in this way are shown in Figs. 5(a) and 5(b) together with corresponding line profiles in Figs. 5(c) and 5(d). Inspection of the graphs suggests that the profiles are significantly different, in agreement with the presence of comparable magnitudes for $\mathrm{Re}(F_0)$ and $\mathrm{Im}(F_0)$.

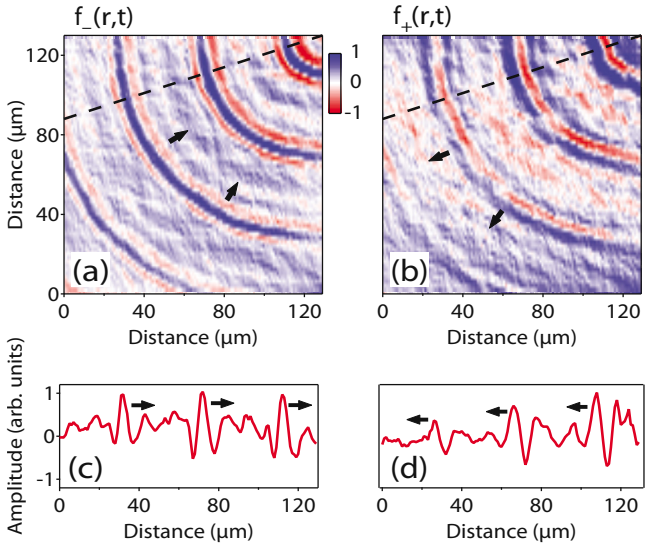


FIG. 5. (Color online) SAW images for (a) converging $[f_-(\mathbf{r},t)]$ and (b) diverging $[f_+(\mathbf{r},t)]$ waves obtained by Fourier analysis at $t=-6$ and +6 ns, respectively. (c) and (d) show wave front profiles taken along the dashed lines in (a) and (b), respectively.

## IV. CONCLUSIONS

In conclusion, we have imaged SAWs in real time on a sphere using an ultrafast interferometric optical technique, and observed their convergence to and divergence from the pole opposite the source. Fourier analysis allows the sound velocity and the source function, that governs the transformation of the wave packet on propagation through the pole, to be extracted. This work suggests that further investigations of thermoelastic SAW generation in a variety of opaque thin films and substrates would be useful to better understand what governs the ratio $\mathrm{Re}(F_0)/\mathrm{Im}(F_0)$. This imaging technique should also prove invaluable for the quality control of SAW ball sensors and should help to elucidate the physics of SAW dispersion and propagation on crystalline spheres.

[1]D. Clorennec and D. Royer, Appl. Phys. Lett. **85**, 2435 (2004).
[2]D. Clorennec and D. Royer, Appl. Phys. Lett. **82**, 4608 (2003).
[3]K. Yamanaka, S. Ishikawa, N. Nakaso, N. Takeda, D. Sim, T. Mihara, A. Mizukami, I. Satoh, S. Akao, and Y. Tsukahara, IEEE Trans. Ultrason. Ferroelectr. Freq. Control **53**, 793 (2006).
[4]H. Yamazaki, O. Matsuda, O. B. Wright, and G. Amulele, Phys. Status Solidi C **1**, 2979 (2004).
[5]H. Yamazaki, O. Matsuda, and O. B. Wright, Phys. Status Solidi C **1**, 2991 (2004).
[6]T. Tachizaki, T. Muroya, O. Matsuda, Y. Sugawara, D. H. Hurley, and O. B. Wright, Rev. Sci. Instrum. **77**, 043713 (2006).
[7]Y. Sugawara, O. B. Wright, O. Matsuda, M. Takigahira, Y. Tanaka, S. Tamura, and V. E. Gusev, Phys. Rev. Lett. **88**, 185504 (2002).
[8]See supplementary material at http://dx.doi.org/10.1063/1.3517076 for material in the form of an animation. RealTimeSphere.mov: a 9700 kB animation of the data for SAWs in the time domain on a glass sphere near the opposite pole from the excitation point. This animation consists of 29 frames over a 12.5 ns time interval, corresponding to the time between two consecutive laser pulses. A $18.3° \times 18.3°$ region of the sphere is imaged. The color scale in this animation is the same as in Fig. 2 in the paper.
[9]T. C. Zhu, H. J. Maris, and J. Tauc, Phys. Rev. B **44**, 4281 (1991).
[10]Y. Sugawara, O. B. Wright, and O. Matsuda, Appl. Phys. Lett. **83**, 1340 (2003).
[11]The exact position of $t=0$ in Fig. 2 was determined by examining the constant frequency surfaces.
[12]G. Farnell and E. L. Adler, Phys. Acoust. **9**, 35 (1972).
[13]A. Neubrand and P. Hess, J. Appl. Phys. **71**, 227 (1992).
[14]H. Lamb, Proc. London Math. Soc. **S1-13**, 189 (1881).
[15]A. Tamura, K. Higeta, and T. Ichinokawa, Solid State Phys. **15**, 4975 (1982).
[16]For BK7 glass, Young's modulus $E=82$ GPa, Poisson's ratio $\nu=0.21$, and density $\rho=2.51$ g cm$^{-3}$, see www.schott.com.
[17]B. A. Auld, *Acoustic Fields and Waves in Solids* (Krieger, Malabar, 1989), Vol. II.
[18]V. Gusev and P. Hess, Appl. Phys. A: Mater. Sci. Process. **61**, 299 (1995).
[19]D. Royer, E. Dieulesaint, X. Jia, and Y. Shui, Appl. Phys. Lett. **52**, 706 (1988).
[20]A. A. Kolomenskii, S. N. Jerebtsov, and H. A. Schuessler, Opt. Lett. **30**, 2019 (2005).
[21]We averaged over all propagation directions in our movie.